Journal of Materials Chemistry

Cite this: DOI: 10.1039/c0jm04442c

www.rsc.org/materials

PAPER

Binder-free $Co(OH)_2$ nanoflake–ITO nanowire heterostructured electrodes for electrochemical energy storage with improved high-rate capabilities

Chaoyi Yan,[a] Hao Jiang,[ab] Ting Zhao,[a] Chunzhong Li,[b] Jan Ma[a] and Pooi See Lee*[a]

Received 19th December 2010, Accepted 26th April 2011
DOI: 10.1039/c0jm04442c

We present the fabrication of binder-free $Co(OH)_2$ nanoflake–ITO nanowire heterostructured electrodes *via* a combination of chemical vapor deposition and electrodeposition methods for electrochemical energy storage applications. Detailed studies showed that the specific capacitance retention capabilities of these hybrid electrodes were greatly enhanced in comparison to electrodes without nanowire augmentation. The improvement was further verified by our statistical studies of electrodes with loading masses in the range of 0–500 μg cm^{-2}. The highly conductive ITO nanowires can serve as direct electron paths during the charge/discharge process, facilitating the full utilization of electroactive materials. These rigid oxide nanowire supports enable facile and uniform surface coating and are expected to be more stable than previous composite electrodes based on carbon nanotubes. This study provides a promising architecture for binder-free electrochemical capacitors with excellent capacitance retention capabilities.

Introduction

Electrochemical capacitors (ECs) are of growing interest as important energy storage devices for potential applications in hybrid electric vehicles and mobile electronic devices.[1–3] ECs exhibit higher power densities and much longer cyclic life than batteries and a higher energy density than conventional dielectric capacitors.[2] Until now, considerable efforts have been devoted to the exploration of high-performance electrode materials, typically including carbonaceous materials,[2,4,5] conducting polymers[6] and metal oxides/hydroxides.[7–9] Carbonaceous materials, such as activated carbon (AC) and carbon nanotubes (CNTs), usually serve as electrical double layer capacitors (EDLCs) with charge stored at the electrode–electrolyte interface. Conducting polymers and metal oxides/hydroxides typically serve as pseudo-capacitors with redox-type charging–discharging processes. However, the low specific capacitances (SCs) of carbonaceous materials and the poor cyclic stability of conducting polymers make them inferior choices compared with metal oxides/hydroxides.

Transition metal hydroxides [such as $Co(OH)_2$ and $Ni(OH)_2$] are of particular interest as high-performance EC electrodes due to their very high theoretical SC values.[9–11] Extensive studies were previously reported on the fabrication of hydroxide electrodes.[9,12–17] However, most of the reports were focused on the enhancement of absolute SC values, and little attention was paid to other attributes, for example, improvement of high-rate capabilities. Severe capacitance degradations at high scan rates/current densities were typically observed in previous reports for metal oxide/hydroxide electrodes.[11,13,18] As an important characteristic in determining the specific power density of ECs, the poor rate performance is a critical issue that remains to be addressed. In this report, we present the synthesis of $Co(OH)_2$ nanoflake (NF)–ITO nanowire (NW) heterostructures by hybrid chemical vapor deposition (CVD) and electrodeposition methods and demonstrate the successful improvement of high-rate capabilities compared with $Co(OH)_2$ NFs directly deposited on planar substrates. The high-quality, binder-free, heterostructured electrodes were shown to be a promising architecture for EC applications with excellent high-rate capabilities.

Experimental

Synthesis of ITO NWs

The ITO NWs were synthesized by the CVD method, in a horizontal double-tube system.[26,27] In a typical experiment, mixed In_2O_3, SnO_2 and carbon powder (weight ratio 9 : 1 : 2) was placed at the sealed end of a small quartz tube (inner diameter 1.5 cm, length 30 cm) as source material. Stainless steel (SS) substrates coated with 9 nm Au film were placed at the open end to collect the products. The small quartz tube was then loaded into the large furnace tube (inner diameter 4 cm, length 1.5 m) with the source material at the high temperature region.[26,27] The central temperature of the furnace was increased to 1000 °C at a rate of 15 °C min^{-1} and kept for 60 min under a constant Ar flow of 50 sccm (standard cubic centimetre per minute). The SS

[a]*School of Materials Science and Engineering, Nanyang Technological University, Singapore, 639798, Singapore. E-mail: pslee@ntu.edu.sg*
[b]*Key Laboratory for Ultrafine Materials of Ministry of Education, East China University of Science & Technology, Shanghai, 200237, China*

substrates were located at the temperature region of 300–400 °C during growth. After growth, the furnace was allowed to cool naturally to room temperature.

Electrodeposition of $Co(OH)_2$ NFs

The $Co(OH)_2$ NFs were deposited uniformly onto the ITO NWs by potentiodynamic electrodeposition in an electrochemical analyzer system (Autolab Potentiostat, PGSTAT302N). The standard 3-electrode cell was used for the electrodeposition, with ITO NW/SS substrate as the working electrode, Pt as the counter electrode and Ag/AgCl as the reference electrode. $Co(NO_3)_2$ solution (0.01 M) was used as the electrolyte. $Co(OH)_2$ was also deposited directly on bare SS substrates for comparative studies. The potentiodynamic deposition was performed with voltage cycling between −0.6 V and −1 V (*vs.* Ag/AgCl) at a scan rate of 100 mV s^{-1}. After deposition, the substrates were washed thoroughly in distilled water and then dried in a vacuum furnace (background pressure 0.01 mbar) at room temperature. The weight of the deposit was measured using a microbalance with an accuracy of 1 μg. Weights of the deposit can be controlled by the deposition cycles.

Characterizations

Morphologies and structures of the ITO NWs and $Co(OH)_2$ NF/ITO NW heterostructures were characterized using scanning electron microscopy (SEM, JEOL 6340F) and transmission electron microscopy (TEM, JEOL 2100F). X-Ray diffraction (XRD) data were collected using a Shimadzu with CuKα radiation ($\lambda = 1.5418$ Å). The chemical compositions were analyzed using energy dispersive spectroscopy (EDS) attached to the TEM system. Electrochemical properties of the $Co(OH)_2$ NFs (without the use of binder or any other carbon additives) were measured using the standard 3-electrode setup, as described above for electrodeposition processes. All the measurements were performed using 1 M KOH electrolyte at room temperature in air.

Results and discussion

Fabrication procedures of the heterostructured $Co(OH)_2$ NF–ITO NW electrodes are schematically shown in Fig. 1. The composite electrodes were fabricated by a combination of CVD and electrodeposition methods. Au was sputtered on a defined area of the SS substrate to catalyze the ITO NW growth. One end of the SS substrate was left open for electrical connection during the following tests. Note that the ITO NWs were well confined within the area coated with Au (Fig. 1 inset, sample 2) because catalysts are essential for the ITO NW growth.[19] $Co(OH)_2$ NFs were then electrodeposited onto the ITO NWs through a potentiodynamic method (with voltages cycling between −0.6 V and −1 V). The deposition mainly occurs at −1 V with high cathodic current, and the voltage scanning process allows buffering time for electrolyte diffusion. Compared with potentiostatic deposition, the potentiodynamic method yields more uniform coatings, ensuring the formation of high-quality "coaxial" $Co(OH)_2$ NF–ITO NW heterostructures (Fig. 3). The loading masses of $Co(OH)_2$ can be easily tuned by changing the deposition cycles. For comparative studies, $Co(OH)_2$ NFs were also deposited directly on bare SS substrates. Later in this study, we use $Co(OH)_2$/NW to represent the $Co(OH)_2$ NF/ITO NW/SS electrodes and $Co(OH)_2$/SS to represent the $Co(OH)_2$ NF/SS electrodes for simplicity.

Morphologies and structures of the ITO NWs were characterized using SEM and TEM. Fig. 2a is a typical cross-sectional SEM image of the as-grown NW "lawns" on a current collector. Dense NWs, with lengths of ~40 μm, grew directly on the substrate surface, *i.e.*, in direct contact with the substrate. Fig. 2b is a high-magnification SEM image of the ITO NWs. The NWs are rigid and well separated, with inter-NW spacings of micrometre scale. These macropores are of great importance to enhance the ionic conductivities, as will be discussed later. Detailed crystallographic structures of the ITO NWs were

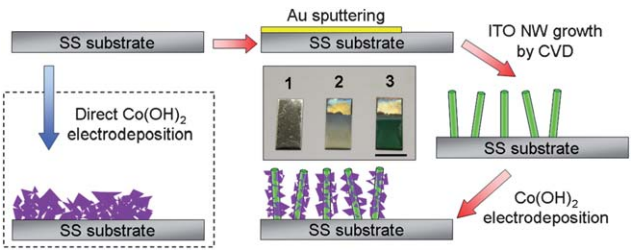

Fig. 1 Schematic models showing the fabrication procedures of $Co(OH)_2$/SS and $Co(OH)_2$/NW electrodes for comparative studies. The $Co(OH)_2$/NW electrodes were fabricated by combinational CVD and electrodeposition methods. The inset is the digital image of Au/SS (sample 1), ITO NW/SS (sample 2) and final $Co(OH)_2$ NF/ITO NW/SS (sample 3). Scale bar is 1 cm.

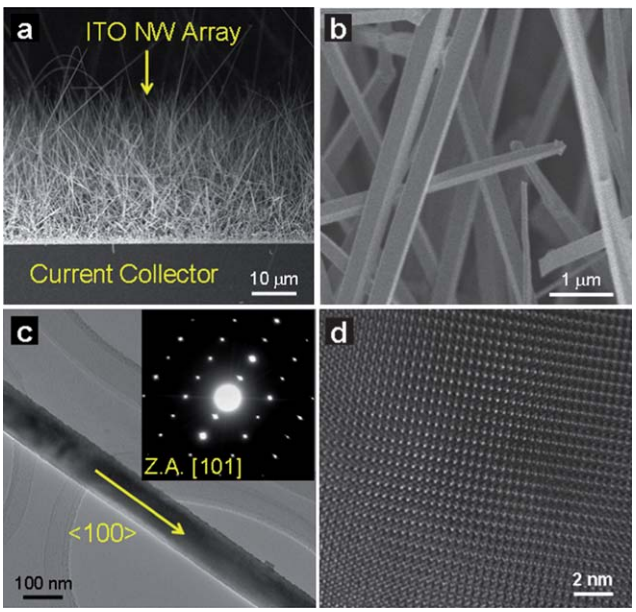

Fig. 2 (a) Cross-sectional SEM image showing the direct contact of ITO NW array with the current collector. (b) High-magnification SEM image showing the rigid ITO NW supports. Microscale macropores were typically observed in the NW arrays. (c) TEM image of an individual ITO NW with smooth surface, growing along ⟨100⟩ direction of the cubic phase. The inset is the corresponding SAED pattern taken along [101] zone axis. (d) HRTEM image of the ITO NW, showing the single-crystalline structures.

characterized using TEM (Fig. 2c and d). Fig. 2c is a low magnification TEM image of an individual NW, showing the smooth surfaces without surface augmentations such as nanoparticles or NFs. The NW is single crystalline growing along the ⟨100⟩ direction of the cubic In_2O_3 phase (JCPDS 06-0416: $a = 10.118$ Å), as verified by the selective area electron diffraction (SAED) pattern (Fig. 2c, inset) and the high-resolution TEM (HRTEM) image (Fig. 2d). Further careful examinations revealed that all of the ITO NWs were single crystalline growing along ⟨100⟩ directions, which is consistent with previous reports.[19]

Fig. 3 shows the structural and chemical composition analysis of the $Co(OH)_2$ NF–ITO NW heterostructures. Potentiodynamic electrodeposition was shown to be a facile and efficient method to achieve high-quality and uniform $Co(OH)_2$ coatings all along the ITO NWs, as shown in Fig. 3a and b. The thickness of the $Co(OH)_2$ shell was typically around 200 nm after 200 deposition cycles. The as-deposited $Co(OH)_2$ NFs are poly crystalline, as revealed by the HRTEM results (Fig. 3c). Instead of the continuous lattice fringes observed for ITO NWs (Fig. 2d), the NF is composed of several nano-grains with different lattice fringe orientations (Fig. 3c). Chemical compositions of the heterostructures were analyzed using EDS attached to the TEM system. An EDS spectrum recorded from the entire $Co(OH)_2$ NF–ITO NW heterostructure is shown in Fig. 3d, revealing the existence of In, Co and O. Peaks of Cu are from the Cu grid used for TEM characterizations. EDS line scanning was performed to demonstrate the elemental distributions of In and Co (Fig. 3e). The scanning path across the heterostructure is indicated by a yellow line in the inset of Fig. 3e. The In element was only observed in the central NW core (red line), and Co was distributed in the surrounding area (blue line). The intensity of Co varied along the scanning path, probably due to the NF folding or overlapping. Morphologies of the $Co(OH)_2$ NFs deposited on bare SS substrates can be found in many previous works.[9,12,16] The measured thicknesses of the $Co(OH)_2$ NFs lie in the range of 5–20 nm under our specific electrodeposition conditions. The ultrathin nanocrystals[28] are highly desired to achieve full utilization of the electroactive materials.

Crystal structures of the hybrid $Co(OH)_2$ NF–ITO NW heterostructures were characterized by XRD (Fig. 4). The diffraction peaks can be readily indexed to two crystal phases: α-$Co(OH)_2$ with rhombohedral structure and In_2O_3 with cubic structure. The six peaks belonging to ITO are indicated by red dash lines, as shown in Fig. 4. Slight peak shifts toward higher angles (0.21°) were observed due to the Sn doping. The three diffraction peaks at 2θ angles of 10.74° [(003) planes], 21.75° [(006) planes] and 33.56° [(012) planes] are the characteristic peaks for layered α-phase $Co(OH)_2$ and were also typically observed for $Co(OH)_2$ nanostructures prepared by electrodeposition.[9,10,12,16,17] Lattice parameters of the as-prepared α-$Co(OH)_2$ are refined to be $a = 3.16$ Å and $c = 24.71$ Å. The calculated interlayer spacing of 24.71 Å is in good agreement with previous reports.[10,20] Taking together the TEM, EDS and XRD results, we

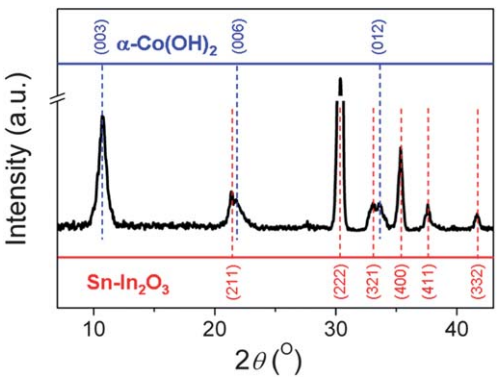

Fig. 4 XRD pattern of the heterostructured $Co(OH)_2$/NW electrodes.

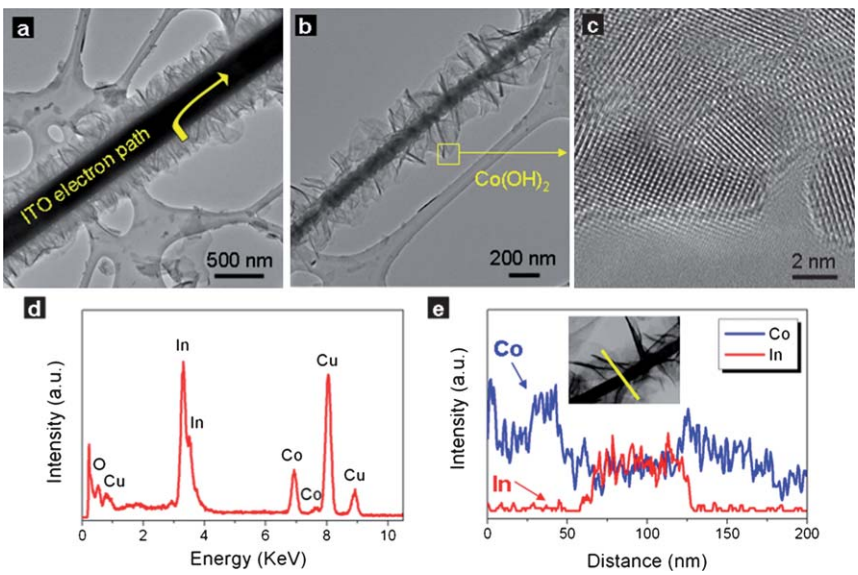

Fig. 3 (a and b) Low magnification TEM images showing the uniform $Co(OH)_2$ coating on the ITO NW surface. (c) HRTEM image of the $Co(OH)_2$ NF showing the polycrystalline structure. (d) EDS spectrum recorded from the entire ITO NW/$Co(OH)_2$ NF heterostructure. (e) EDS line scanning result showing the elemental distributions of Co and In.

conclude that high-quality $Co(OH)_2$ NF–ITO NW heterostructures with homogeneous $Co(OH)_2$ NF coatings were successfully synthesized. Those composite electrodes possess excellent hierarchical architectures for EC applications, with layered α-$Co(OH)_2$ NFs as electroactive materials and ITO NWs as direct electron "highways" to the current collector.

The capacitive properties of the as-prepared electrodes were measured using the cyclic voltammetry (CV) method. CV responses of two representative $Co(OH)_2$/SS and $Co(OH)_2$/NW electrodes, with loading masses of 384 μg and 323 μg, are shown in Fig. 5a and b, respectively. It should be highlighted that we used two electrodes with similar loading masses of $Co(OH)_2$ for performance comparison because the EC performances are mass-dependent (as will be shown in Fig. 7). Fig. 5a contains the CV responses of a $Co(OH)_2$/SS electrode measured using 1 M KOH aqueous electrolyte within the potential range of −0.15 V to 0.35 V at different scan rates. Distinct from EDLCs, which would produce CV curves close to a rectangular shape, strong redox peaks were observed for the pseudo-capacitive $Co(OH)_2$/SS electrode, especially at slower scan rates. The reduction (−0.02 V, with positive current) and oxidation (−0.11 V, with negative current) peaks (scan rate 5 mV s^{-1}) can be attributed to the following Faradaic reactions:[9]

$$Co(OH)_2 + OH^- \underset{\text{reduction}}{\overset{\text{oxidation}}{\rightleftharpoons}} CoOOH + H_2O + e^- \quad (1)$$

The SC values at different scan rates have been calculated from the CV curves using the following equation:

$$SC = \frac{Q}{mV}(F/g) \quad (2)$$

where Q is the discharge amount, m is the $Co(OH)_2$ loading mass and V is the potential window. Calculated SC values of the $Co(OH)_2$/SS electrodes at 5, 10, 20, 50 and 100 mV s^{-1} scan rates are 585, 506, 411, 278, and 195 F g^{-1}, respectively. Similar CV characteristics were also observed for the $Co(OH)_2$ NW electrode (Fig. 5b). Calculated SC values of the $Co(OH)_2$/NW electrodes at 5, 10, 20, 50 and 100 mV s^{-1} scan rates are 622, 613, 588, 530 and 450 F g^{-1}, respectively.

As shown in Fig. 5a and b, the shapes of the CV curves depend on the scan rates. The shape change can be described using two parameters: peak current (i_p) and peak potential separation (ΔE_p). Taking the $Co(OH)_2$/NW electrode (Fig. 5b) as an example, the anodic peak current, i_p, increases from 0.006 to 0.025, 0.053, 0.107 and 0.161 A at scan rates of 5, 10, 20, 50 and 100 mV s^{-1}, respectively. Additionally, the peak potential separations, ΔE_p, are 0.07, 0.1, 0.15 and 0.26 V for scan rates of 5, 10, 20 and 50 mV s^{-1}, respectively. The oxidation peak at 100 mV s^{-1} is out of the potential range and thus is not included. Similar shape changes were exclusively observed for all the $Co(OH)_2$/SS and $Co(OH)_2$/NW electrodes and can be attributed to two possible reasons. First, the electrochemical reactions (eqn (1)) are quasi-reversible, deviating from the ideal reversible/Nernstian behaviors. As previously demonstrated, both theoretically and experimentally, the peak current and peak potential separation for quasi-reversible reactions would increase at higher scan rates.[21] However, for reversible/Nernstian reactions, peak potential separation is independent of scan rates, with only peak current being proportional to $v^{1/2}$, where v is the scan rate. Second, the uncompensated potential drops (IR drop) would also contribute to the peak potential separation. It was shown that the IR drop effect is qualitatively similar to the kinetic effect of quasi-reversible reactions.[21,22] The IR drop increases at higher scan rates due to the larger current density. Additionally, the higher scan rates allow less time for efficient electrolyte diffusion and reaction, *i.e.*, larger ionic diffusion resistances. The increased

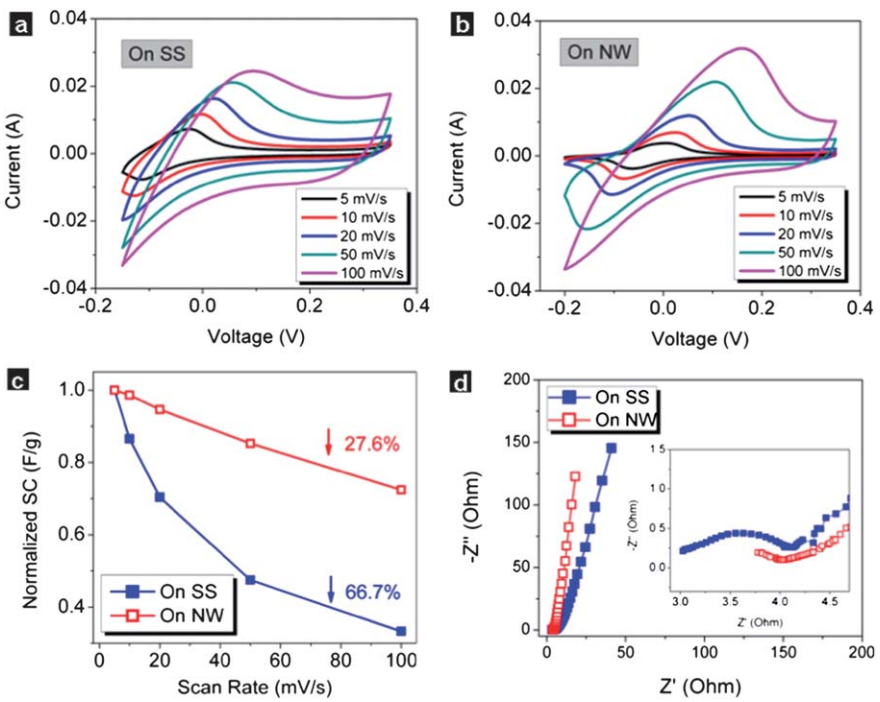

Fig. 5 Comparative (a and b) CV plots, (c) normalized SC *versus* scan rate and (d) complex-plane impedance spectra for the $Co(OH)_2$/SS and $Co(OH)_2$/NW electrodes.

electrode and electrolyte resistances coupled with the likely insufficient active material involved in the redox reactions all contribute to the lower SC values at higher scan rates (Fig. 5c).

The focus of the present work is to demonstrate the enhanced high-rate capability of the heterostructured $Co(OH)_2$/NW electrodes by forming superior hierarchical structures. We use SC degradation to characterize the capacitance retaining capabilities of the electrodes, which is calculated as follows:

$$\text{SC degradation} = \frac{SC_5 - SC_{100}}{SC_5} \quad (3)$$

where SC_5 and SC_{100} are the SC values at 5 and 100 mV s^{-1} scan rates, respectively. Fig. 5c shows the normalized SC as a function of scan rates for the two electrodes. While the SC degradation for the $Co(OH)_2$/SS electrode is as large as 66.7%, only 27.6% degradation was observed for the $Co(OH)_2$/NW electrode. A comparison of those two samples clearly reveals the improved high-rate capacitance retaining capabilities of the $Co(OH)_2$/NW electrode, which was later further reinforced by our statistical studies (Fig. 7).

The improved high-rate capabilities of the $Co(OH)_2$/NW electrode can be attributed to the hierarchical geometry of the heterostructures, which is advantageous in electron transport. In the heterostructured electrode, each NF is directly connected to the ITO NW stem, which serves as a facile electron path for charge transport. Thus, the ITO NW arrays grown on a current collector allow efficient electron conduction during charging/discharging processes. This improved electron conduction significantly enhances the conductivity of the electroactive materials. However, for compact $Co(OH)_2$ NFs deposited on planar SS substrates, facile electron transport can only be achieved in the bottom layer (in direct contact with the current collector). Electron transport from the top layers to the current collector is hindered due to the poor conductivity of the $Co(OH)_2$ NFs and possibly inter-flake contact resistances. The distorted multi-segment conduction paths for $Co(OH)_2$/SS electrode are schematically shown in Fig. 6a. As discussed above, the large electrode resistance would lead to poor SC performances. This effect would be exaggerated at higher scan rates (Fig. 5c) and higher loading masses (Fig. 7). For example, the SC values for the $Co(OH)_2$/SS (Fig. 5a) and $Co(OH)_2$/NW (Fig. 5c) electrodes at 5 mV s^{-1} are 585 and 622 F g^{-1}, respectively. However, the corresponding SC values are 195 and 450 F g^{-1} at a higher scan rate of 100 mV s^{-1}, indicating a more prominent SC drop for the $Co(OH)_2$/SS electrode, probably due to the large resistance. Analogously, degradation is also expected to increase with loading masses due to the increased layer thicknesses and, hence, increased resistances (Fig. 7).

Equivalent series resistances (ESRs) of the two types of electrodes were measured to verify the conductivity enhancement, as shown in the complex plane electrochemical impedance spectra (EIS, Fig. 5d). The loading masses of the $Co(OH)_2$/SS and $Co(OH)_2$/NW electrodes were 292 μg and 316 μg, respectively. The measurements were performed at a dc bias of 0 V with a sinusoidal signal of 5 mV over the frequency range from 30 kHz to 0.01 Hz. The straight segments at lower frequencies can be attributed to the capacitive behavior of the electrode, and the semicircular loop at higher frequencies (Fig. 5d, inset) is due to charge-transfer resistances of the electrodes. The diameter of the semicircular loop (*i.e.*, ESR) for the $Co(OH)_2$/SS electrode (1.06 Ω) is larger than that of the $Co(OH)_2$/NW electrode (0.23 Ω) under the same measurement conditions. The smaller ESR for the $Co(OH)_2$/NW electrodes reveals unambiguously the enhanced charge transfer capabilities for the $Co(OH)_2$ NFs in those heterostructured electrodes.

The mass-dependent SC degradation behaviors were also investigated, as shown in Fig. 7. Fourteen $Co(OH)_2$/SS electrodes and ten $Co(OH)_2$/NW electrodes with different loading masses in the range of 0–500 μg were synthesized for comparative studies of degradation–mass relationships. Multiple samples were used to reveal the statistical behaviors, minimizing the effect of measurement errors and sample-to-sample variations. The measured degradation values are represented by filled [$Co(OH)_2$/SS electrodes] and open [$Co(OH)_2$/NW electrodes] squares in Fig. 7, and the corresponding solid lines are the linear

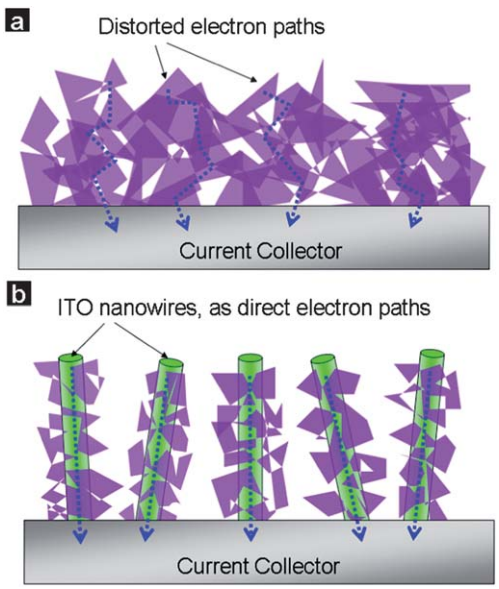

Fig. 6 Schematic models showing the distorted electron conduction for NF stacks in $Co(OH)_2$/SS electrodes and the role of ITO NWs as direct electron paths in $Co(OH)_2$/NW electrodes.

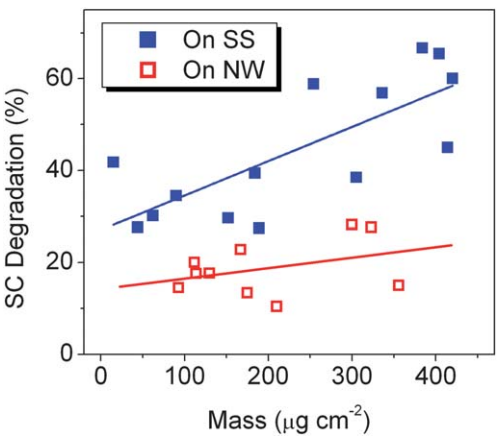

Fig. 7 SC degradation value *versus* loading mass plot for the $Co(OH)_2$/SS (blue filled square) and $Co(OH)_2$/NW (red open square) electrodes.

fitting curves. Several notable features can be observed in the plot. First, degradation increases with loading masses for both $Co(OH)_2$/SS and $Co(OH)_2$/NW electrodes. The thicknesses of the $Co(OH)_2$ layers increase with loading masses, and the even longer and severely distorted electron conduction paths result in larger electrode resistances. Consequently, the SC degradation value increases due to the more significant IR drops at higher scan rates, as well as the lower utilization of the active materials, as have been discussed for the two electrodes in Fig. 5a and b. The slope of the fitting curve for the $Co(OH)_2$/SS electrodes (7.5% per 100 μg) is larger than that of the $Co(OH)_2$/NW electrodes (2.3% per 100 μg), suggesting a faster degradation trend *vs.* loading mass. Second, a clear trend of reduced SC degradation, *i.e.*, improved SC retaining capabilities at higher scan rates, can be observed for $Co(OH)_2$/NW electrodes. For example, $Co(OH)_2$/NW electrodes with 400 μg active material exhibited SC degradation of 23%, but the value is as large as 57% for $Co(OH)_2$/SS electrodes with the same loading mass (calculated from the fitting curve). Third, statistical results from multiple samples help to reveal a more accurate mass–degradation relationship, and this is of critical importance because the measured SC degradation values exhibited relatively large variations, even for similar loading masses (Fig. 7). Notably, statistical EC performances, in most cases, have not been reported in previous studies.

Finally, we discuss our results and compare with literature in the following aspects. First, the well-separated ITO NWs with robust mechanical properties provide rigid support for the $Co(OH)_2$ NFs. The microscale macropores in the NW lawn provide buffering reservoirs for electrolytes, minimizing the ionic diffusion distances. This ensures high ionic conductivity for the composite electrode. However, for $Co(OH)_2$/SS electrodes, only facile electrolyte access to the top layer is ensured. Large ionic diffusion resistances may be observed, especially at high loading masses, resulting in increased SC degradations (Fig. 7). Second, hydrothermal precipitation has also been frequently used for the preparation of $Co(OH)_2$ nano-powders, which were then mixed with carbon black and binders for EC applications.[14,17,23] However, this method requires much more time-consuming processes than electrodeposition, such as solution aging, powder filtering, surfactant removing, powder mixing (with carbon and binder) and drying. Moreover, simple mechanical stirring of the paste mixture[14] during electrode preparation cannot ensure a homogeneous distribution of active materials. The agglomerates (usually of micrometre dimensionalities) would lead to inferior performances due to poor electrochemical accessibility and lower ionic conductivity. In contrast, electrodeposition is a facile method for electrode preparation. In particular, the as-prepared $Co(OH)_2$/NW electrodes with improved electron conductivity and firm contact with the ITO NW/SS current collector adopt the advantages of carbon black (increase the conductivity) and polymer binder (increase the contact conditions) while successfully prevent the agglomeration problem. Third, some studies have previously reported using CNTs to enhance the electrical conductivity of redox-capacitive materials [such as MnO_x, $Ni(OH)_2$, and CoOOH] for EC applications.[2,8,13,24] However, direct synthesis of uniform CNT/redox-capacitive material heterostructures through electrodeposition is rather difficult due to the intact and smooth CNT surfaces and their poor solubility in solvents.[24] As a result, instead of uniform coatings on CNT surfaces, only agglomerated nanoflowers or large-size grains were observed.[8,13,24] On the contrary, ITO NW surfaces with sufficient dangling bonds lead to uniform $Co(OH)_2$ coating all along the NW stem (Fig. 3). These high-quality "coaxial" heterostructures lead to a higher utilization of the active materials and, hence, higher performances. Additionally, compared with CNTs, the oxide-based supports are more chemically and thermally stable, which is especially desired for potential applications, for example, at elevated temperatures and in oxygen abundant environments. Fourth, although investigations of the performances of hydroxide electrodes at different scan rates/current densities can be found in some previous reports, lateral comparison of the absolute degradation values was found to be difficult due to the different scan rates/current density ranges, a lack of corresponding SC values and, more importantly, a lack of loading masses.[9,14,15,23–25] Nevertheless, the comparative studies in present work revealed, self-consistently, the improved high-rate capabilities of $Co(OH)_2$ NFs through the formation of hierarchical heterostructures.

Conclusions

In conclusion, we demonstrated the hybrid synthesis of $Co(OH)_2$ NF–ITO NW heterostructures for EC applications with improved high-rate capabilities. A combination of CVD and electrodeposition methods was used to synthesize the nanoscale heterostructures. Unlike CNTs, uniform coating of electroactive materials all along the ITO NW surface can be easily achieved, ensuring the formation of high-quality heterostructures and, hence, excellent performances. CV characterizations showed that the capacitance degradation of the $Co(OH)_2$/NW electrodes at higher scan rates was successfully improved compared with $Co(OH)_2$/SS electrodes. This improvement was attributed to the enhanced electrode and electrolyte conductivities originating from the unique hierarchical architectures with each electroactive NF directly connected to the current collector. The statistical comparative studies provide solid evidence for the performance improvement. The designing of nanoscale heterostructures, illustrated by combining the advantages of electroactive $Co(OH)_2$ NF and highly conductive ITO NWs, is a promising strategy for future electrode engineering.

Acknowledgements

The authors thank Lu Xiaowei and Yan Xiaowen for their support and insightful discussions. C.Y.Y. thanks NTU for research scholarship.

References

1 B. E. Conway, *Electrochemical Supercapacitors: Scientific Fundamentals and Technological Applications*, Kluwer Academic/Plenum Publishers, New York, 1999.
2 P. Simon and Y. Gogotsi, *Nat. Mater.*, 2008, **7**, 845.
3 J. Chmiola, C. Largeot, P. L. Taberna, P. Simon and Y. Gogotsi, *Science*, 2010, **328**, 480.
4 E. Frackowiak and F. Beguin, *Carbon*, 2001, **39**, 937.
5 C. M. Niu, E. K. Sichel, R. Hoch, D. Moy and H. Tennent, *Appl. Phys. Lett.*, 1997, **70**, 1480.

6 A. Rudge, J. Davey, I. Raistrick, S. Gottesfeld and J. P. Ferraris, *J. Power Sources*, 1994, **47**, 89.
7 H. Kim and B. N. Popov, *J. Power Sources*, 2002, **104**, 52.
8 H. Zhang, G. P. Cao, Z. Y. Wang, Y. S. Yang, Z. J. Shi and Z. N. Gu, *Nano Lett.*, 2008, **8**, 2664.
9 V. Gupta, T. Kusahara, H. Toyama, S. Gupta and N. Miura, *Electrochem. Commun.*, 2007, **9**, 2315.
10 Z. P. Liu, R. Z. Ma, M. Osada, K. Takada and T. Sasaki, *J. Am. Chem. Soc.*, 2005, **127**, 13869.
11 G. W. Yang, C. L. Xu and H. L. Li, *Chem. Commun.*, 2008, 6537.
12 V. Gupta, S. Gupta and N. Miura, *J. Power Sources*, 2008, **177**, 685.
13 C. G. Liu, Y. S. Lee, Y. J. Kim, I. C. Song and J. H. Kim, *Synth. Met.*, 2009, **159**, 2009.
14 L. B. Kong, J. W. Lang, M. Liu, Y. C. Luo and L. Kang, *J. Power Sources*, 2009, **194**, 1194.
15 D. D. Zhao, S. J. Bao, W. H. Zhou and H. L. Li, *Electrochem. Commun.*, 2007, **9**, 869.
16 V. Gupta, S. Gupta and N. Miura, *J. Power Sources*, 2008, **175**, 680.
17 Z. A. Hu, Y. L. Xie, Y. X. Wang, L. J. Xie, G. R. Fu, X. Q. Jin, Z. Y. Zhang, Y. Y. Yang and H. Y. Wu, *J. Phys. Chem. C*, 2009, **113**, 12502.
18 T. Y. Wei, C. H. Chen, K. H. Chang, S. Y. Lu and C. C. Hu, *Chem. Mater.*, 2009, **21**, 3228.
19 Q. Wan, E. N. Dattoli, W. Y. Fung, W. Guo, Y. B. Chen, X. Q. Pan and W. Lu, *Nano Lett.*, 2006, **6**, 2909.
20 M. S. Yarger, E. M. P. Steinmiller and K. S. Choi, *Chem. Commun.*, 2007, 159.
21 A. J. Bard and L. R. Faulkner, *Electrochemical Methods: Fundamentals and Applications*, John Wiley & Sons, Inc., 2nd edn., 2001.
22 R. S. Nicholso, *Anal. Chem.*, 1965, **37**, 1351.
23 C. Z. Yuan, X. G. Zhang, B. Gao and J. Li, *Mater. Chem. Phys.*, 2007, **101**, 148.
24 B. Gao, C. Z. Yuan, L. H. Su, L. Chen and X. G. Zhang, *J. Solid State Electrochem.*, 2009, **13**, 1251.
25 W. J. Zhou, J. Zhang, T. Xue, D. D. Zhao and H. L. Li, *J. Mater. Chem.*, 2008, **18**, 905.
26 N. Singh, T. Zhang and P. S. Lee, *Nanotechnol.*, 2009, **20**, 195605.
27 C. Y. Yan and P. S. Lee, *J. Phys. Chem. C*, 2009, **113**, 14135.
28 H. B. Zeng, C. Y. Zhi, Z. H. Zhang, X. L. Wei, X. B. Wang, W. L. Guo, Y. Bando and D. Golberg, *Nano Lett.*, 2010, **10**, 5049.